Carbon 262 (2027) 122234

Contents lists available at ScienceDirect

Carbon

journal homepage: www.elsevier.com/locate/carbon

Surface reconstruction governs graphene epitaxy on sapphire

S. Forti [a,*], D. Acharya [b], D. Perilli [b], N. Mishra [a,1], A.A. Zakharov [c], C. Di Valentin [b], C. Coletti [a]

[a] Center for Nanotechnology Innovation, Istituto Italiano di Tecnologia, Piazza San Silvestro 12, Pisa, 56127, Italy
[b] Department of Materials Science, University of Milano-Bicocca, Via R. Cozzi 55, Milano, 20125, Italy
[c] MAX IV Laboratory, University of Lund, Lund, 22100, Sweden

A B S T R A C T

The direct growth of single-crystal graphene on dielectric substrates is highly appealing for semiconductor technologies, particularly in optoelectronics. Sapphire (α-Al_2O_3(0001), c-plane) is a platform holding great promise, yet graphene growth on this surface remains poorly understood and often results in rotational disorder and mosaicity. A key source of ambiguity is that the role of the surface reconstruction, ubiquitous under growth conditions, is often overlooked. In this work, we provide experimental and theoretical results that clearly indicate how graphene epitaxy on sapphire is governed by the reconstructed interface. Specifically, we show that two low-strain commensurate configurations of graphene on the most stable surface reconstruction under growth conditions, the $(\sqrt{31}\times\sqrt{31})R\pm9^\circ$, account for the majority of experimentally observed domains. We further suggest an alternative interpretation in which the frequently observed R30 orientation may emerge from the convolution of nearby commensurate domains, yielding a unified picture of graphene growth on sapphire. Our results highlight interface control as the key requirement for achieving flat, strain-free graphene with epitaxially constrained orientations on sapphire, and establish a consistent framework to interpret the observed graphene aligned R30 with respect to the sapphire (1×1), as well as its distributed mosaicity.

1. Introduction

Graphene has the potential to become a key material in next generation communication and quantum technologies, owing to its exceptional electronic properties and compatibility with CMOS platforms. In this perspective, understanding how to achieve ordered, single-layer graphene on sapphire is not merely an open materials-science challenge, but a key requirement for enabling large-scale graphene integration. In the past fifteen years several groups have attempted different strategies to attain large-area high-quality graphene on c-plane sapphire [1–4]. Despite these efforts, graphene grown on α- Al_2O_3(0001) consistently exhibits rotational disorder and mosaicity, ranging from oligo-to polycrystalline, even when macroscopic film quality and transport properties appear promising.

A major source of ambiguity is that graphene growth on sapphire is often discussed in terms of the bulk-terminated substrate, while the reconstructions formed at interface under growth conditions are rarely treated as the primary degree of freedom. This omission is critical, because α-Al_2O_3(0001) undergoes substantial reconstruction upon thermal treatment [5], and the resulting interface ultimately defines the epitaxial template for graphene. In other words, understanding graphene on sapphire requires first the understanding and controlling its reconstructed interface.

Among the various reconstructions, the $(\sqrt{31}\times\sqrt{31})R\pm9^\circ$ (which we will call r31 throughout the text), first observed in the late 1960s [6,7], is the most thermodynamically stable, and the most frequently observed under graphene growth conditions [1,8]. Despite extensive theoretical and experimental efforts [9–11], its detailed atomic structure has only recently been resolved [12] and it was shown to be flatter and with better local order than the unreconstrucuted surface [13]. However, its role in determining graphene orientation and mosaicity remains largely unexplored.

Here, we combine density functional theory (DFT) with a comprehensive set of surface-sensitive techniques to identify configurations that stabilize graphene on the r31 interface and assess their relevance in real samples. In particular, we show that two least-strain commensurate structures account for the majority of experimentally observed domains. We further propose an alternative interpretation of the observed long the 30° orientation with respect to sapphire (R30) orientation [1,3], showing that the diffraction signal might emerge from the convolution of nearby commensurate domains associated with the reconstructed interface.

* Corresponding author.
E-mail address: stiven.forti@iit.it (S. Forti).
[1] Present address: CamGraPhiC Technologies, Pisa (IT).

https://doi.org/10.1016/j.carbon.2026.122234
Received 20 August 2026; Received in revised form 11 October 2026; Accepted 19 October 2026
Available online 20 October 2026
0008-6223/© 2026 The Authors. Published by Elsevier Ltd. This is an open access article under the CC BY license (http://creativecommons.org/licenses/by/4.0/).

2. Methods

2.1. Computational details

Density functional theory (DFT) calculations were performed using the *Quantum ESPRESSO* package [14] to investigate the interaction between graphene and the two structural variants, O-poor and O-rich, of the ($\sqrt{31} \times \sqrt{31}$)R±9° Al_2O_3(0001) surface reported experimentally by Hütner et al. [12]. The optimized surface unit cell has an in-plane lattice parameter of 26.5 Å. Exchange–correlation effects were treated within the generalized gradient approximation using the Perdew–Burke–Ernzerhof (PBE) functional [15]. Core–valence electron interactions were described using ultrasoft pseudopotentials [16]. Electronic wavefunctions were expanded in a plane-wave basis set with kinetic energy cutoffs of 40 Ry for the wavefunctions and 400 Ry for the charge density. Because the interaction between graphene and Al_2O_3 is dominated by van der Waals forces, dispersion corrections were included via the DFT + D3 scheme [17]. Brillouin-zone sampling was performed using a 2 × 2 × 1 Monkhorst–Pack k-point mesh [18] for the ($\sqrt{31} \times \sqrt{31}$)R±9° surface.

The choice of the exchange–correlation functional, plane-wave energy cutoffs, and k-point sampling was based on extensive convergence and validation tests performed for bulk and unreconstructed α-Al_2O_3(0001) surface and interface with Gr in our recent study [19]. In the present work, which exclusively considers the reconstructed α-Al_2O_3(0001) surface, the corresponding computational parameters were adapted to the larger reconstructed model based on the validated setup.

The slab model of Al_2O_3(0001) consists of three regions: (i) a reconstructed surface layer containing the Al and O atoms that form the ($\sqrt{31} \times \sqrt{31}$)R ± 9° pattern, (ii) an interface layer connecting the surface reconstruction to the underlying bulk-like structure, and (iii) two additional bulk-like layers. A vacuum region of 20 Å was included along the surface normal to prevent spurious interactions between periodic images. The bottom of the slab was passivated with hydrogen atoms to eliminate dangling bonds and suppress artificial polarization effects associated with asymmetric slab termination. During structural relaxation, the interface layer and the first bulk layer beneath it were allowed to fully relax, whereas the bottommost bulk layer and the hydrogen atoms were kept fixed.

To investigate the interaction between graphene and the ($\sqrt{31} \times \sqrt{31}$)R±9° Al_2O_3(0001) surface, we considered two relative angular orientations of graphene that minimize the lattice mismatch with the substrate. In the first configuration, graphene is rotated by 13.9° with respect to the reconstructed Al_2O_3 surface cell, resulting in a compressive mismatch of 0.66%. In the second configuration, graphene is rotated by 19.1°, leading to a tensile mismatch of 1.5%. In both cases, the graphene sheet remains flat after structural optimization. The lattice mismatch values (0.66% for the 13.9° rotation and 1.5% for the 19.1° rotation) were computed from the lattice parameters of Gr and Al_2O_3(0001) optimized at 0 K and are intended only as an indication of the relative commensurability of the two configurations. Since Gr and Al_2O_3 show opposite thermal behavior [20–22], and Gr forms at high temperature during CVD and is then cooled, no single temperature-dependent mismatch is uniquely representative; moreover, the weak Gr/substrate interaction allows part of the strain to be released through wrinkles or defects.

To compute the charges on atoms, partitioning the electron charge density is done by the Bader charge analysis [23]. To analyze and visualize the interfacial electron charge redistribution, we computed the differential electron charge density, defined as:

$$\Delta\rho = \rho_{\text{graphene+Al2O3}} - \left(\rho_{\text{Al2O3}} + \rho_{\text{graphene}}\right)$$

where $\rho_{\text{graphene +Al2O3}}$ is the total electron charge density of the combined system, ρ_{Al2O3} is the electron charge density of the isolated Al_2O_3 slab, ρ_{graphene} is the electron charge density of the isolated graphene sheet. The interfacial electron charge density will be presented as two-dimensional plots.

Scanning tunneling microscopy (STM) simulations were carried out using the Tersoff–Hamann approximation [24], in which the tunneling current is proportional to the energy-integrated local density of states (ILDOS). The constant-current and bias voltage values for the STM simulations were chosen to match the experimental values. Structural visualizations and ball-and-stick models were generated using the VESTA software package [25]. Energy decomposition analysis was carried out following a procedure previously developed in our works [26,27].

2.2. Graphene growth

Substrate preparation and graphene growth were carried out following the procedures described in Ref. [1]. Specifically, before growth, sapphire substrates were cleaned with acetone, isopropanol, and deionized (DI) water in an ultra-sonicator bath, immersed in piranha solution (1:3, H_2O_2:H_2SO_4) for 15 min, and finally washed in DI water and N_2-blow-dried. Graphene was directly grown on c-plane sapphire substrates, from Roditi International Corporation Ltd with ±0.5° unintentional miscut towards m-plane, by chemical vapor deposition (CVD) in a commercial Aixtron Black Magic showerhead reactor, without the use of a metal catalyst. Prior to graphene growth, the sapphire substrates were subjected to an H_2 etching treatment at 1180 °C for 5 min under a continuous H_2 flow of 1000 sccm at 750 mbar. This treatment regularizes the surface from chemo-mechanical polishing, resulting in an ordered step-terrace morphology. In addition, due to the highly reducing atmosphere, it promotes surface reconstruction, as reported in Refs. [1] and [28]. The H_2-etched sapphire substrates were subsequently used for the direct growth of graphene using CH_4 as the carbon precursor. Graphene growth was performed at 1130 °C for 10 min at 25 mbar in an Ar/H_2/CH_4 atmosphere with flow rates of 1000, 150, and 5 sccm, respectively. The samples were cooled down under Ar flow 1000 sccm for approximately 90 min.

2.3. STM

Scanning Tunneling Microscopy (STM) measurements were carried out in a Omicron LT-STM at 78 K using a tungsten tip produced by electrochemical etching.

2.4. LEED

Low-Energy Electron Diffraction (LEED) measurements were performed at room temperature using a Specs ErLEED 150 system.

2.5. LEED profile analysis

We defined an annular intensity profile along the entire azimuth defined by the graphene spots of the LEED image and took the mean on a ±30° angular range, centered on the maximum of the intensity. We then converted the x-coordinate from angle to parallel momentum, so that $k_{||} = \vartheta k_{gr}$. The profiles were then offset-subtracted and normalized to 1. For each of these average intensity profiles, we carried out a fit with four gaussian components: one very broad and weak to take into account the inelastic background contribution, two side components to account for the contribution of the Gr aligned on the r117 and a central one to account for the R30-Gr. The positions of the components were allowed little displacements, while the widths were essentially left free. The error-bars in Fig. 4 b and c are ±10% on the widths, while they are ±12% for the ratios in panel d.

2.6. LEEM and μLEED

Low-Energy Electron Microscopy (LEEM) and selected-area (SA)-LEED (or μLEED) measurements were done at the MAXPEEM beamline of the MAX-IV synchrotron facility in Lund, Sweden. The instrument was an Elmitec LEEM microscope.

2.7. ARPES

Angle-resolved photoemission spectroscopy measurements were obtained on a Specs Flex system, using a He plasma micro-Sirius UV light lamp and an Astraios 190 electron analyzer, equipped with deflector lenses.

3. Results and discussion

At the high temperatures required to synthesize graphene, sapphire undergoes a series of surface reconstructions [11], the most stable being the $(\sqrt{31}\times\sqrt{31})R9^{\circ}$, which for brevity we call r31. To determine how graphene can be accommodated on this structure, we computed the coincidence site lattice (CSL) structures between graphene and the r31 reconstruction, allowing for both strain and rotational misalignment between the two (see Section 1 of SI). Of all the solutions, two configurations are of particularly low strain $|\varepsilon|<2\%$, whereas all the other structures involve higher strain and are therefore less likely to be thermodynamically relevant under typical growth conditions. These structures can be expressed in Wood's notation [5] as $(3\sqrt{13}\times3\sqrt{13})R13.9$ and $(4\sqrt{7}\times4\sqrt{7})R19.1$ (hereafter referred to as r117 and r112) and represent the minimal strain solutions for graphene accommodation on r31. Density functional theory (DFT) calculations were employed to determine their relaxed structure and the energetics of adsorption, adhesion and strain [19], on both O-poor and O-rich variants of the r31 reconstructions, with the calculated energetics reported in Table S2. In the following, we focus on the O-poor case [12], as it represents the most physically relevant scenario under typical growth conditions – i.e., reducing gases and high temperatures [1] – and is consistent with the experimental observations presented later in the paper. Fig. 1(a) (e) and (b) (f) show the top and side views of the r117 (r112) configuration, respectively. For the r117, the lattice mismatch is 0.66%, with graphene slightly compressed to match the surface supercell, whereas for the r112, the lattice mismatch is 1.5% and graphene is slightly stretched. Among the two, the r117 configuration exhibits the lowest lattice mismatch and is therefore expected to be energetically favored, although at 1500 K they are essentially equivalent. After optimization, the graphene layer remains flat with a vertical separation of 3.20 Å and 3.12 Å from the substrate for r117 and r112, respectively. The corresponding charge density and PDOS (Fig. 1(c), (d), (g), (h)) reveal localized electron accumulation on specific regions of the graphene layer, consistent with simulated scanning tunneling microscopy (STM) images (cf. Fig. 3). In both configurations, the Dirac cone is shifted to the left of the Fermi level (Fig. 1(d) and (h)), indicating n-type doping in graphene. This is further confirmed by Bader charge analysis, which yields electron accumulation values of 0.84 e and 1.04 e per repeating cell for the r117 and r112 configuration, respectively. In contrast, analogous calculations performed for the O-rich r31-reconstructed surface indicate p-type doping of graphene (see SI). The consistent observation of n-type doping across literature reports [1,2,29] and in the ARPES data presented later in this work supports the validity of the O-poor reconstruction under graphene growth conditions.

To verify the theoretical findings, we performed multiple spectroscopic and microscopic measurements on graphene grown on sapphire via chemical vapor deposition (CVD) [1,28]. Before growth, we carried out a high-temperature annealing step in a reducing atmosphere, which is known to promote the formation of the r31 reconstruction on the sapphire surface [1,8,28]. Notably, this reconstruction has been reported under a variety of preparation conditions, including in the absence of hydrogen annealing [9] and even following oxygen exposure [12], indicating that the thermodynamic path is not unique and it does not strictly depend on the preparation protocol used. The low-energy electron microscopy (LEEM) micrograph shown in Fig. 2a is representative of the typical morphology of graphene grown on sapphire and reveals a distribution of graphene domains with distinct contrast, reflecting different crystallographic orientations. Consistently, the low-energy electron diffraction (LEED) pattern exhibits a graphene-related intensity distribution, with stronger signal around the R30 direction with respect to the sapphire vectors (Fig. 2b). The spots about the (00) reflex are covered by the electron gun, but can be clearly visualized in μLEED imaging, where two threefold symmetric hexads of spots become evident (inset in panel b). To identify the origin of the different diffraction features, we first compare the experimental LEED data with a synthetic pattern (Fig. 2c), constructed from 2D Gaussian profiles centered on the diffraction spots associated with the r117 and r112 graphene configurations, the r31 reconstruction, and the sapphire (1×1) lattice (see section 4 in the SI for details). To disentangle the contributions of the different components, we then consider the corresponding kinematic LEED pattern (Fig. 2d), where the diffraction spots associated with sapphire (red), the r31 reconstruction (grey), and graphene (blue and purple) are explicitly identified using the results derived in Section 1 of the SI. The hexads are attributed to the R9 and R−9 domains of the r31, indicating that the substrate is consistently terminated by r31 beneath graphene. The graphene spots coming from the r117 and r112 structures, over the two r31 domains, i.e. eight patterns (cf. Fig. S1 and relative discussion) are sufficient to justify the great majority of the observed spots. Not always all spots predicted by the kinematic model are experimentally resolved, possibly due to a combination of instrumental effects, overlap of diffraction intensities, lower statistical occurrence of specific domains or an internal symmetry of the unit cell that leads to systematic extinction of the reflex. In particular, the spots at R30 $\pm$ 1.9° and $\pm$7.1° are well represented, while those near R0$\pm$4.9° and $\pm$10.1° are less frequently observed (see SI).

We would like to point out that in LEED, the diffracted intensity from graphene, appears along a circumference, rather than on a distorted hexagon, as one would expect from the kinematic model in Fig. 2d. This is due to several reasons: first of all, the required graphene strain ranges from 0.6 to 1.5%, while our experimental resolution is of the order of 3% (see Sections 4 and 5 in SI). Moreover, despite locking into commensurate structures at high temperatures, graphene will tend to relax its lattice during the cool down, so that the matching with the underlying reconstruction will only be approximate. This is an effect due to the difference of thermal expansion coefficient (TEC) – which is large between graphene and sapphire – and has been already observed [30] and that is accentuated by the fact that graphene has a large negative TEC [20]. In addition, at growth temperatures, the commensurate structures are potentially all energetically accessible. As a consequence, graphene will have several domains as well as a high density of grain boundaries and dislocations, within the spot of the LEED electron beam (which is approximately 1 mm across).

Unlike Gr/Cu(111) [31], where the small lattice mismatch allows a quasi-continuum of orientations to be accommodated through strain, on the r31 the equilibrium orientations are pinned to a discrete commensurate set (cf. section 1 of the SI). The observed azimuthal spread is therefore not of thermodynamic origin but rather due to the high number of line-defects, which contribute to the azimuthal disorder, as they provide a wide range of local crystal lattice orientations, which in turn increase the azimuthal smearing of the diffraction spots. The effect resulting from this azimuthal broadening is well reproduced in Fig. 2 c, where the high intensity at R30 is the result of the sum of the R30 $\pm$ 1.9° spots from the r112 structure (see Discussion and SI).

We performed selected area (SA)-LEED on single domains with reference to Fig. 2a and we always see the r31 reconstruction terminating the c-plane sapphire. Notably, in most cases, we can model the orientations of the graphene/r31 with only few solutions of the static

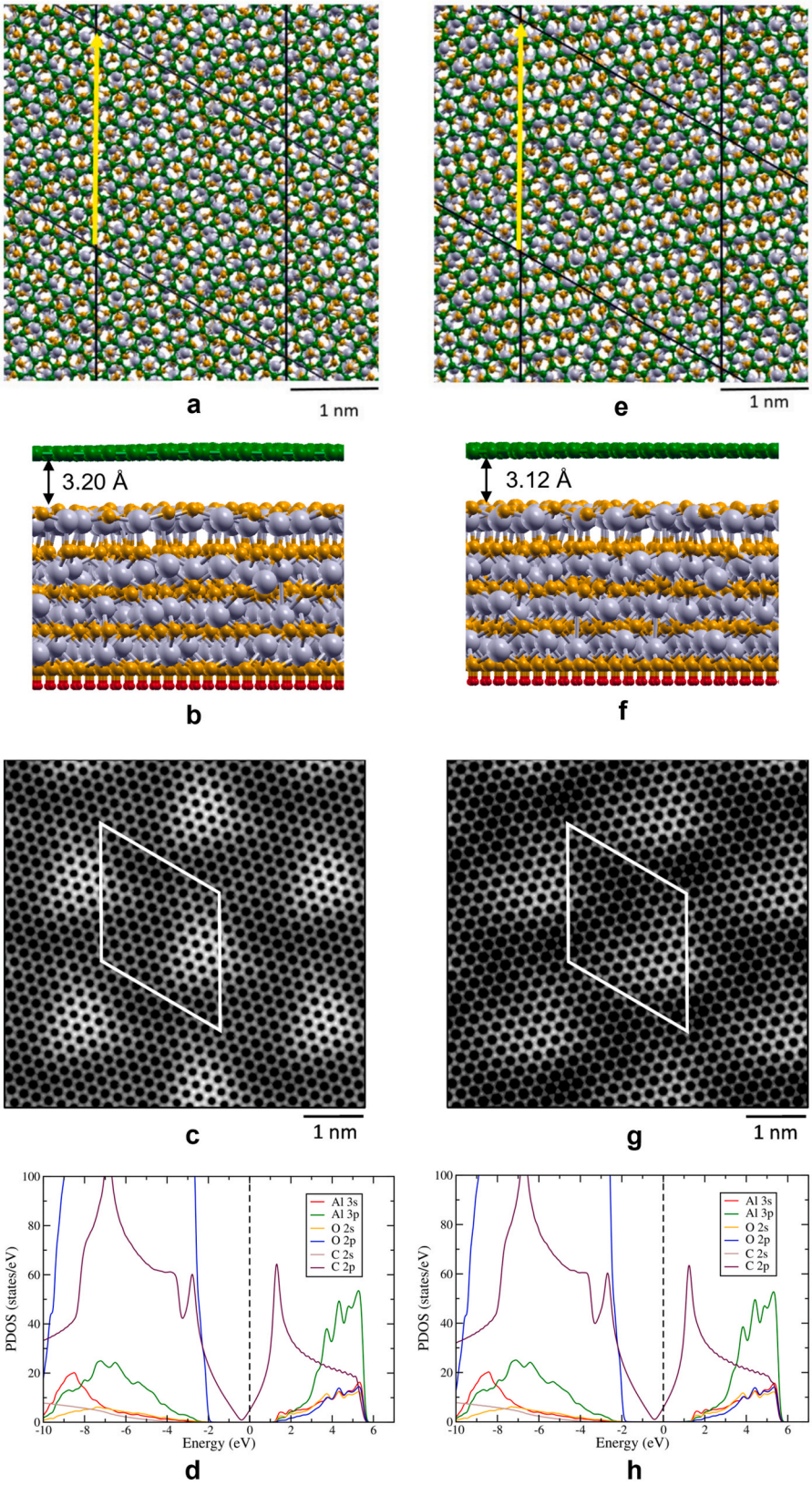


Fig. 1. Low-strain coincidence structures, two-dimensional electron charge density plot and total/projected density of states of graphene/r31 for the O-poor system: (a-d) r117; (e-h) r112.

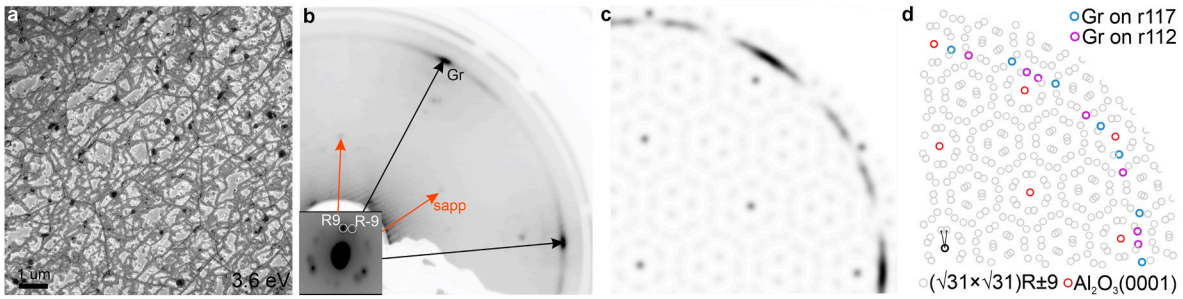


Fig. 2. Graphene domain distribution over c-plane sapphire. a LEEM micrograph measured at 3.6 eV over a 10 μm field of view (FOV). b LEED recorded at 67 eV. In the inset: μLEED at 60 eV with contrast aperture 100 μm, showing the intensity about the (00) spot. c Synthetic LEED pattern. d kinematic LEED patterns of sapphire, ($\sqrt{31}\times\sqrt{31}$)R±9° and graphene (r117 and r112 structures). The ($\sqrt{31}\times\sqrt{31}$)R±9° spots are grey, red the sapphire (1×1), while graphene's are blue and purple. (For interpretation of the references to colour in this figure legend, the reader is referred to the Web version of this article.)

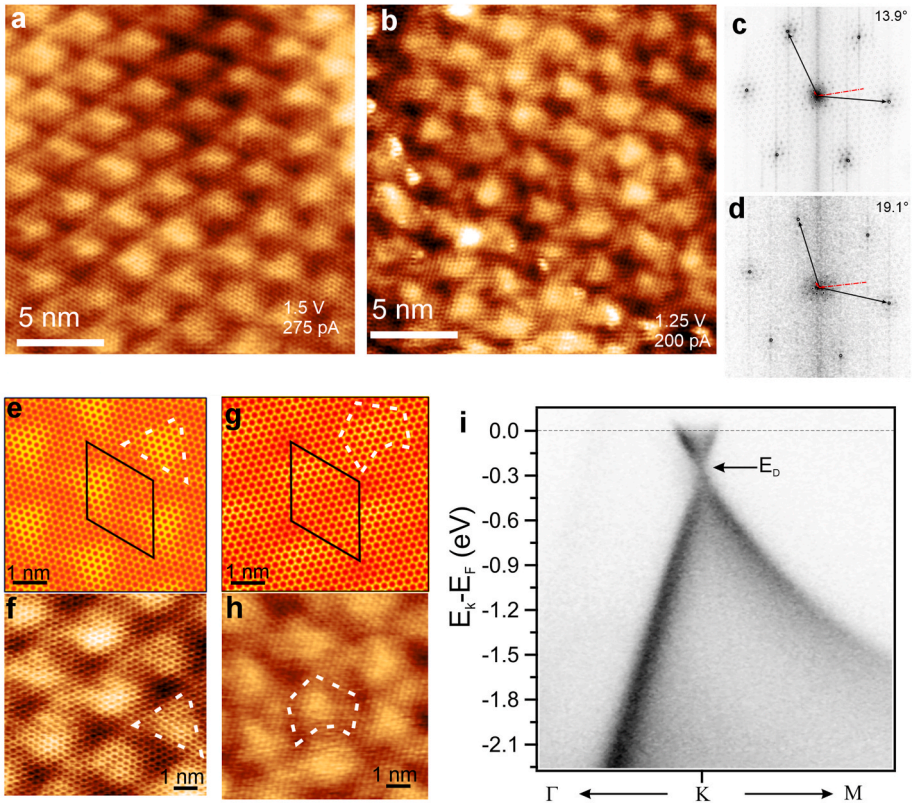


Fig. 3. Structural and electronic properties of graphene/r31/sapphire. **a** STM on Gr/r117. **b** STM on Gr/r112. **c** 2D-FFT of panel **a**. **d** 2D-FFT of panel **b**. **e** simulated pseudo-height map of Gr/r117. **f** measured STM on Gr/r117. **g** simulated pseudo-height map of Gr/r112. **h** measured STM on Gr/r112. **i** ARPES spectrum of Gr/r31/sapphire. The simulated STM images in panels (e) and (g) were calculated at a bias of 0.5 V.

model showed in the SI (see Figs. S1 and S9).

Local measurements of the sample's morphology, such as STM, reveal a scenario supporting the hypothesis that sees the minimal strain structures as more frequent. In Fig. 3a and b, we display two 20 × 20 nm^2 areas – collected on two different regions of the same sample – with atomic resolution, clearly showing a 26.5 Å periodic modulation due to the r31 reconstruction underneath graphene. However, performing the 2D fast-Fourier transform (FFT) of the images, we can discern some differences. Panels c and d show the 2D-FFT of images a and b, respectively. The mutual orientation between graphene and the r31 is marked on the panel and it is measured to be (14 ± 1)° in the case of the region in panel a and (19 ± 1)° in the region shown in panel b, indicating the r117 and r112 configurations, respectively. In the FFT images, the red line indicates the orientation of the r31 reconstruction. It should be noted that its orientation does not change in the two regions. What changes is the relative orientation of graphene, indicated in the panel by the black vectors. We detect the different local arrangement of the graphene's atoms with respect to its substrate also by looking at the pseudo-height distribution in more detail. The experimental maps (f and h) can be compared with the simulated maps (e and g) for the same two structures. The resemblance between the simulated and the measured, in the case of the r117 is apparent. We can clearly appreciate the difference in the pseudo-height map geometry between panels f and h, and note that panel h is much more closely related to the intensity distribution simulated in panel g than e. The electronic properties of graphene were probed by means of angle-resolved photoemission spectroscopy (ARPES), which we report in panel i. From those measurements, we can estimate the position of the Dirac energy E_D and locate it at 270 meV from the Fermi level, compatible with the simulated value shown in Fig. 1 d and h (DOS plots). In several publications about graphene

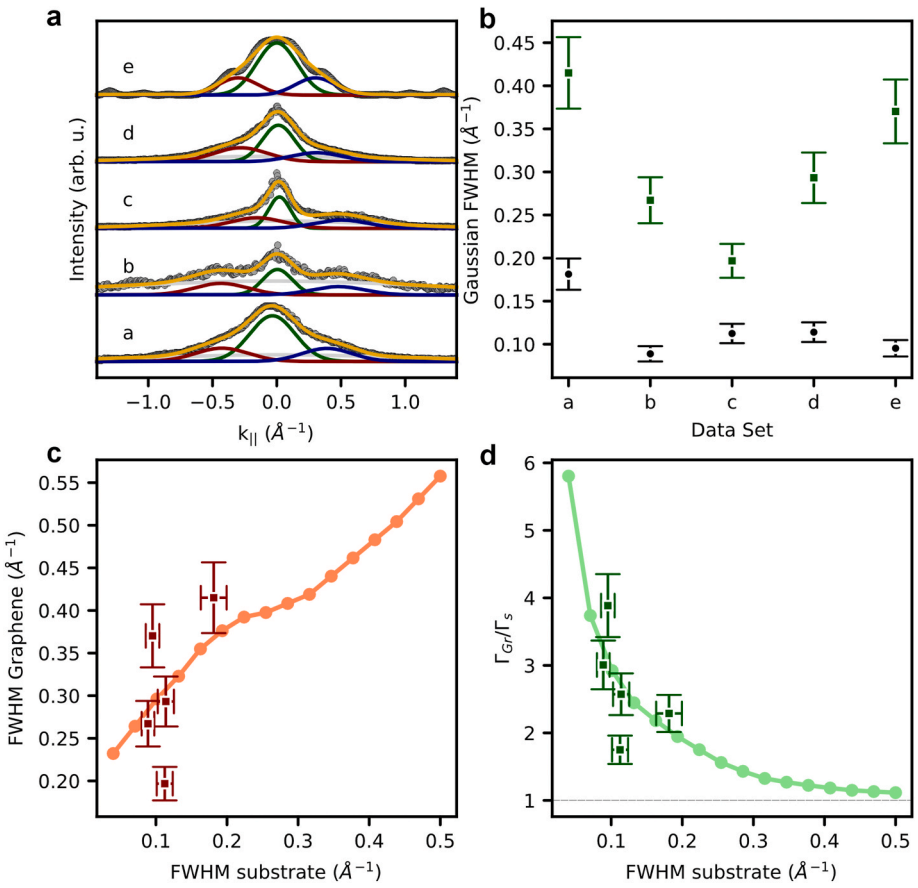


Fig. 4. Analysis of the R30-Gr LEED spot width. a Azimuthal intensity profile taken and averaged along the graphene reciprocal lattice vector (cf. Fig. S5 and its description) on the data reported in Fig. S5 a-e **b** single LEED spot width (black circles) and the width of the R30-Gr component (green squares) per each data set. **c** theoretical trend of Γ_G vs w (coral cirlces) and the same trend for the experimental and synthetic datasets (red squares). **d** theoretical trend of the Γ_G/w vs w (green circles) and the same trend for the experimental and synthetic data sets (green squares). (For interpretation of the references to colour in this figure legend, the reader is referred to the Web version of this article.)

directly grown onto $Al_2O_3(0001)$, the most frequently observed orientation of graphene with LEED is usually the R30, with respect to the sapphire (1×1) [1,3,28]. Theory (based on DFT calculations) predicts that graphene could arrange on the unreconstructed surface with a commensurate structure of $(9\sqrt{3}\times9\sqrt{3})$R30 graphene on (8×8) sapphire, maintaining a very low level of strain and a mild adsorption distance with respect to the substrate's surface [19] (see Fig. S3 for comparing the different kinematic LEED models associated to each superperiodicity). Experimentally, we do not have evidence of graphene growing as a single R30 domain on the (1×1) $Al_2O_3(0001)$ and forming that long-range superperiodicity. Occasionally, we have observed patches of graphene growing on metastable surface reconstruction, i.e. the $(3\sqrt{3}\times3\sqrt{3})$R30 [5] or r27, which is naturally commensurate with graphene, as it deviates from a graphene (10×10) by only the 0.5% (cf. Fig. S4). This configuration would represent a natural template for graphene to grow aligned R30 with respect to the substrate, but it appears to be a very rare and statistically not relevant event. In addition, we could observe a clean r27 LEED pattern only on H-etched surfaces, but not upon graphene growth, indicating that – if present – it covers a very small area of the sample. For graphene to grow atop the r31 aligned R30 with the substrate, we find that the smallest coincidence lattice transformation matrix to realize that is $\begin{vmatrix} 7 & -4 \\ 4 & 11 \end{vmatrix}$, or $\left(\sqrt{3}\sqrt{31} \times \sqrt{3}\sqrt{31}\right)R21$, but it requires an almost 12% of biaxial tensile strain on the graphene lattice. We therefore consider it very unlikely to happen.

To gain deeper insight into the possible origin of the R30-graphene (R30-Gr) feature, we analyze a representative set of LEED patterns (Fig. S5) acquired from different samples, spanning a range of inelastic background and azimuthal disorder. This ensures that the analysis captures the variability typically observed in graphene grown on sapphire. From 4 experimental LEED patterns and a synthetic data set (cf. Fig. S5), we extract the average azimuthal intensity profile of the R30-Gr spots (see Methods) within a ±15° range and fit them with four gaussian components. The results of this fitting – converted into reciprocal-space – are shown in ZWHM of the substrate diffraction spots (G_s), shown as black circles, and the width of the central component (green curve in Fig. 4a) used to fit the annular R30-Gr intensity (G_{Gr}), shown as green squares. Notably, G_{Gr} is more than twice as wide as the substrate spots G_s. Such broadening is strictly azimuthal and not radial, ruling out possible strain inhomogeneities (radial broadening) as well as small crystalline patches (isotropic broadening). Hence, only rotational disorder remains, which leads us to read the apparent R30 feature as originating from the superposition of multiple nearby components [32]. From the kinematic LEED analysis (Fig. 2d), the closest diffraction spots are located symmetrically at approximately R30 ± 1.9° with respect to sapphire (cf. Table S1). To test whether this angular separation could account for the observed R30-Gr feature, we model the R30-Gr intensity as the sum of two Gaussian components centered at these positions. A Gaussian of the form $G(x, x_1, x_2, s) = G_1(x, x_1, s) + G_2(x, x_2, s)$, i.e. given by the sum of two Gaussians, becomes undistinguishable from a single peak when the distance between the maxima $dx = |x_2\text{-}x_1|$ is comparable or smaller than the width of each component $w = 2\sqrt{2\ln 2}\sigma \cong 2.35\sigma$. For $dx < w$, the resulting profile exhibits a single maximum located at $(x_2\text{-}x_1)/2$ and the fine structure of the two contributions is no longer

resolved (cf. Fig. S6). This corresponds to an angular separation of 3.8°, which, along the circumference defined by the graphene reciprocal lattice vector on the LEED detector, corresponds to 0.195 $Å^{-1}$, in good agreement with the experimentally extracted G_{Gr} values (red squares). In panel **c** we show G_{Gr} as a function of the G_s (red squares), together with the values calculated for G_G as a function of w (light-red dotted line). Panel **d** shows the ratio G_{Gr}/G_s as a function of G_s (green squares) compared with the expected G_G/w dependence (light-green dotted line), showing good overall agreement between experiment and model. The angular separation required to reproduce the observed broadening matches the expected positions of diffraction spots associated with the r117 and r112 graphene configurations. This provides a direct link between the apparent R30 intensity and the underlying commensurate domains stabilized on the reconstructed r31 interface, indicating that the commonly observed R30 feature can naturally emerge from the superposition of nearby diffraction contributions rather than reflecting a single, well-defined graphene orientation.

A recent work based on nc-AFM and DFT shows that the unreconstructed Al_2O_3(0001)-(1×1) surface is not an atomically flat and uniform Al-terminated template, but is instead rough and laterally inhomogeneous, with only nanoscale ordered regions [13]. By contrast, the thermodynamically stable $(\sqrt{31}\times\sqrt{31})R\pm9°$ reconstruction forming at high temperatures provides a much flatter and better ordered surface. This picture is consistent with our previous observations that graphene grown on unreconstructed or poorly reconstructed sapphire is polycrystalline, whereas preferential alignment is obtained when the r31 reconstruction is present [1,28]. In the work of Hütner et al. [12], the r31 surface is prepared under highly controlled conditions and is only slightly stoichiometrically unbalanced. In our case, the high-temperature annealing in a strongly reducing H_2 atmosphere likely favors an oxygen-deficient interfacial r31 phase (see Methods), as also indicated by our previous works [1,28], and in other works using similar parameters [33]. Nevertheless, we consistently observed the r31 superperiodicity beneath graphene and that appears to act as the relevant epitaxial template.

We should add that the surface landscape of the c-plane sapphire under graphene growth conditions is intrinsically complex, both chemically and morphologically. At high temperatures, a crystal surface can undergo severe transformations, such as roughening or step bunching, both driven by defect diffusion and capable of strongly restructuring the surface through the proliferation of atomic steps [34–36]. While leaving the local crystalline order and stoichiometry intact, these processes limit long-range coherence and favor the coexistence of multiple equivalent epitaxial orientations, thereby shaping the observed mosaicity of graphene. Surface phase transitions and instabilities are most likely accompanied by defect formation under out-of-equilibrium conditions, which may be further promoted during our hydrogen-annealing step [1,28]. In this regime, surface evolution is governed by kinetic mechanisms, ranging from step-flow dynamics [37] to large-scale kinetic roughening [38].

In this paper, we rationalize this complexity by providing a justification for the observed mosaicity of graphene on the r31. We provide another example of Gr/r31/Al_2O_3(0001) in Fig. S8 a, where we show the STM data across two sapphire terraces and a structure connected to the step-edge. The synthesis of graphene on sapphire is an out-of-equilibrium process, which can locally produce instabilities of the surface caused by larger oxygen desorption. Hence we would attribute this kind of structure to inhomogeneity in the sapphire decomposition during the annealing phase. Similar structures have been interpreted as partially decoupled graphene [8], but no detailed information about the interface were provided. Recently we have discussed the kinetics of the spontaneous decoupling process of graphene on sapphire [28]. On a larger scale, the net resulting domain distribution can be appreciated in Fig. 1a (and also Fig. S8b). A more detailed analysis of the domains is reported in Fig. S9, where we display small FOV-LEEM, together with LEEM-IV reflectivity and SA-LEED from single domains. On those domains, we always observe the r31 with either R9 or R-9 orientations with respect to sapphire, and we can model the measured pattern with one of the superstructures mentioned above, i.e. the r117 or the r112, and we also find the presence of the $\left(\sqrt{109}\times\sqrt{109}\right)R24.5$ (or r109, cf. Section 1 and Fig. S9 in SI), which contributes to the LEED pattern with spots at 30 ± 3.5°, only 1.6° from the r112, hence having both the effects of increasing the intensity and the broadening of the R30-Gr signal. LEEM-IV reflectivity (LEER) curves provide some deeper insight. The bright islands display a LEER trace compatible with a single layer graphene and an interface layer, i.e. the r31 reconstruction. The inter-domain regions appear to be exhibiting at least a dip more, if not two. Such a behavior could indicate both the presence of local bilayer graphene or a double interface layer [39,40] and their morphology is most likely identified by the rough area in Fig. S8a.

The orientation of graphene single-crystal domains may in principle be set at nucleation, e.g. by nuclei docking at substrate steps, as reported for hBN on vicinal metal surfaces [41], or by the energetics of the graphene–substrate interface. The two scenarios are not mutually exclusive, since energy differences between competing registries enter the nucleation barrier and are exponentially amplified during nucleation and growth [42]. While our data do not resolve the nucleation stage, two observations point to the interface registry as the selecting factor. On our wafers the step edges run on average along $\langle 11\bar{2}0\rangle$, parallel to the surface lattice vectors, so that step-templated nucleation would favor orientations locked to the substrate lattice [43], such as R0, which is instead systematically depleted. Moreover, the observed orientations $\varphi = \vartheta \pm 9°$ follow the chirality of the underlying r31 domains, as expected if the registry with the reconstruction determines the orientation. Therefore, considering the thermodynamic instability and the intrinsic short-range disorder of the unreconstructed c-plane surface, understanding high-quality graphene growth on sapphire most likely requires identifying the stable graphene configurations on the r31. Within this framework, the mosaicity commonly observed in graphene on sapphire can be understood as arising from a discrete set of energetically favorable configurations. The small energy difference between the r117 and r112 configurations allows both orientations to be populated during high-temperature growth, leading to azimuthal disorder that remains constrained to specific epitaxial relationships rather than forming a purely random distribution. At the same time, the low strain associated with these configurations may explain why relatively high carrier mobilities have been reported in graphene on sapphire, even in the presence of apparent mosaicity [29]. Also, the origin of the commonly observed R30 feature in LEED can be reconsidered. Indeed, theory predicts a low-strain commensurate structure for graphene on unreconstructed Al_2O_3(0001), that is a $(9\sqrt{3}\times9\sqrt{3})R30$ of graphene sits on a (8×8) of sapphire and provides least strain angle at ±3.2° and 30° (cf. Fig. S3). Experimentally, however, we appear to always observe the presence of the r31 at the interface. We therefore suggest to model the typical LEED pattern of graphene on sapphire, which yields a piece of arc about the R30, as the convolution of the R28.1 and R31.9 spots, which stem from the graphene on the r112. Looking at the line profile displayed in Fig. 4, we see that the symmetric broadening of the intensity profile is well described by the presence of the R22.9 and R37.1 spots, belonging to the r117 structure.

This interpretation reconciles the widespread observation of R30-like features [3,12,15] with the absence of a corresponding low-strain commensurate structure on the reconstructed surface.

4. Conclusions

In this work, we discuss about graphene accommodating several commensurate structures on the r31 and those act as an epitaxial registry, thereby unveiling the reason behind the well-known rotational disorder and mosaicity of graphene grown on α- Al_2O_3(0001). On the most stable and relevant reconstruction under growth conditions, the

r31, we find that the two statistically more frequent configurations are the r117 and r112, which are the two minimal-strain structures. Density functional theory predicts that graphene can grow essentially flat and strain-free on those structures, and our experimental results confirm both their structural and electronic properties. Hence, the rotational disorder and mosaicity commonly observed in graphene on sapphire can be understood as the result of a discrete set of energetically favorable commensurate configurations, rather than as a purely random distribution of orientations. Furthermore, by quantitatively analyzing the diffraction spot profiles, we suggest that the commonly observed R30 feature does not necessarily correspond to a single, well-defined graphene orientation but instead emerges from the convolution of diffraction contributions associated with the r117 and r112 domains. Our results establish the reconstructed interface as the key degree of freedom controlling graphene orientation on sapphire and provide a quantitative framework for interpreting diffraction data. They also indicate where the interface could be engineered, as extensively done for graphene on copper [44–46]. Since each commensurate registry occurs on both the R+9° and R−9° domains of the r31, favouring a single chirality of the reconstruction would halve the number of accessible orientations; and since several registries are energetically competitive, tuning the stoichiometry of the reconstruction, which our calculations show to affect the interface, may shift their balance. More broadly, they highlight the central role of interface engineering in achieving controlled synthesis of graphene on sapphire, with implications extending to other 2D and bulk materials.

CRediT authorship contribution statement

S. Forti: Writing – review & editing, Writing – original draft, Visualization, Validation, Methodology, Investigation, Formal analysis, Data curation, Conceptualization. **D. Acharya:** Writing – original draft, Visualization, Software, Data curation, Investigation. **D. Perilli:** Writing – review & editing, Writing – original draft, Visualization, Validation, Data curation, Investigation, Formal analysis. **N. Mishra:** Writing – review & editing, Methodology, Investigation. **A.A. Zakharov:** Validation, Methodology, Investigation, Data curation. **C. Di Valentin:** Writing – review & editing, Writing – original draft, Validation, Supervision, Resources, Project administration, Funding acquisition, Conceptualization, Formal analysis, Methodology. **C. Coletti:** Writing – review & editing, Writing – original draft, Supervision, Resources, Project administration, Funding acquisition, Conceptualization.

Declaration of competing interest

The authors declare that they have no known competing financial interests or personal relationships that could have appeared to influence the work reported in this paper.

Acknowledgements

The authors would like to thank Prof. Ulrich Starke for his valuable insights and technical comments about the LEED measurements and Dr. Yuran Niu for providing a critical review of the manuscript.

S.F. and C.C. acknowledge funding from the European Union Horizon Europe research and innovation program under grant agreement No. 101130384 (QUONDENSATE) and PNRR MUR Project PE000023 CUP J53C22003200005 National Institute of Quantum Science and Technology (NQSTI) funded by the European Union—Next Generation EU. D.A., D. P., and C. D. V. acknowledge funding from the European Union, NextGenerationEU, through the Italian Ministry of University and Research under PNRR (M4C2I1.4 ICSC), Centro Nazionale di Ricerca in High Performance Computing, Big Data and Quantum Computing (Grant No. CN00000013 and Innovation Grant ASGARD with Leonardo and Ferrovie dello Stato).

Appendix A. Supplementary data

Supplementary data to this article can be found online at https://doi.org/10.1016/j.carbon.2026.122234.

References

[1] N. Mishra, et al., Wafer-scale synthesis of graphene on sapphire: toward fab-compatible graphene, Small 15 (2019) 1904906.
[2] M.A. Fanton, et al., Characterization of graphene films and transistors grown on sapphire by metal-free chemical vapor deposition, ACS Nano 5 (2011) 8062.
[3] Z. Chen, et al., Direct growth of wafer-scale highly oriented graphene on sapphire, Sci. Adv. 7 (2021) eabk0115.
[4] J. Tang, C.Y. Kang, L.M. Li, H.B. Pan, W.S. Yan, S.Q. Wei, P.S. Xu, Graphene grown on sapphire surface by using SiC buffer layer with SSMBE, Phys. Procedia 32 (2012) 880.
[5] M. Gautier, J.P. Duraud, L. Pham Van, M.J. Guittet, Modifications of α-Al_2O_3(0001) surfaces induced by thermal treatments or ion bombardment, Surf. Sci. 250 (1991) 71.
[6] T.M. French, G.A. Somorjai, Composition and surface structure of the (0001) face of α-alumina by low-energy electron diffraction, J. Phys. Chem. 74 (1970) 2489.
[7] C.C. Chang, LEED studies of the (0001) face of α-Alumina, J. Appl. Phys. 39 (1968) 5570.
[8] H. Wördenweber, S. Karthäuser, A. Grundmann, Z. Wang, S. Aussen, H. Kalisch, A. Vescan, M. Heuken, R. Waser, S. Hoffmann-Eifert, Atomically resolved electronic properties in single layer graphene on α-Al_2O_3(0001) by chemical vapor deposition, Sci. Rep. 12 (2022) 18743.
[9] J.V. Lauritsen, M.C.R. Jensen, K. Venkataramani, B. Hinnemann, S. Helveg, B. S. Clausen, F. Besenbacher, Atomic-scale structure and stability of the $\sqrt{31}\times\sqrt{31}$R9° surface of Al_2O_3(0001), Phys. Rev. Lett. 103 (2009) 8.
[10] G. Renaud, B. Villette, I. Vilfan, A. Bourret, Atomic structure of the α-Al_2O_3(0001) ($\sqrt{31}\times\sqrt{31}$) R±9°reconstruction, Phys. Rev. Lett. 73 (1994) 1825.
[11] M. Gautier, G. Fenaud, L. Pham Van, B. Villette, M. Pollak, N. Thromat, F. Jollet, J.-P. Duraud, α-Al_2O_3(0001) surfaces: atomic and electronic structure, J. Am. Ceram. Soc. 77 (1994) 323.
[12] J.I. Hütner, A. Conti, D. Kugler, F. Mittendorfer, G. Kresse, M. Schmid, U. Diebold, J. Balajka, Stoichiometric reconstruction of the Al_2O_3(0001) surface, Science 385 (2024) 1241.
[13] J.I. Hütner-Reisch, A. Conti, D. Kugler, F. Mittendorfer, M. Schmid, U. Diebold, J. Balajka, AFM imaging reveals the unreconstructed α-Al_2O_3(0001) surface to be inhomogeneous and rough, Nat. Commun. 17 (2026) 4692.
[14] P. Giannozzi, et al., Quantum ESPRESSO: a modular and open-source software project for quantum simulations of materials, J. Phys. Condens. Matter 21 (2009) 395502.
[15] J.P. Perdew, S. Kurth, A. Zupan, P. Blaha, Accurate density functional with correct formal properties: a step beyond the generalized gradient approximation, Phys. Rev. Lett. 82 (1999) 2544.
[16] A. Dal Corso, Density functional perturbation theory for lattice dynamics with fully relativistic ultrasoft pseudopotentials: application to fcc-Pt and fcc-Au, Phys. Rev. B 76 (2007) 054308.
[17] J. Moellmann, S. Grimme, DFT-D3 study of some molecular crystals, J. Phys. Chem. C 118 (2014) 7615.
[18] H.J. Monkhorst, J.D. Pack, Special points for Brillouin-zone integrations, Phys. Rev. B 13 (1976) 5188.
[19] D. Acharya, D. Perilli, D.V. Cristiana, Optimizing the G raphene/α-Al_2O_3(0001) interface through minimization of interfacial stress for improved electronic applications, ACS Appl. Nano Mater. 8 (2025) 22626.
[20] D. Yoon, Y.-W. Son, H. Cheong, Negative thermal expansion coefficient of graphene measured by Raman spectroscopy, Nano Lett. 11 (2011) 3227.
[21] W.M. Yim, R.J. Paff, Thermal expansion of AlN, sapphire, and silicon, J. Appl. Phys. 45 (1974) 1456.
[22] M. Pozzo, D. Alfè, P. Lacovig, P. Hofmann, S. Lizzit, A. Baraldi, Thermal expansion of supported and freestanding graphene: lattice constant versus interatomic distance, Phys. Rev. Lett. 106 (2011) 135501.
[23] G. Henkelman, A. Arnaldsson, H. Jónsson, A fast and robust algorithm for Bader decomposition of charge density, Comput. Mater. Sci. 36 (2006) 354.
[24] J. Tersoff, D.R. Hamann, Theory of the scanning tunneling microscope, Phys. Rev. B 31 (1985) 805.
[25] K. Momma, F. Izumi, VESTA 3 for three-dimensional visualization of crystal, volumetric and morphology data, J. Appl. Crystallogr. 44 (2011) 1272.
[26] D. Perilli, et al., CO adsorption on a single-atom catalyst stably embedded in graphene, Angew. Chem. 137 (2025) e202421757.
[27] L. Ferrighi, D. Perilli, D. Selli, C. Di Valentin, Water at the interface between defective graphene and Cu or Pt (111) surfaces, ACS Appl. Mater. Interfaces 9 (2017) 29932.
[28] N. Mishra, et al., Spontaneous intercalation of graphene on sapphire, Small Methods 10 (2026) e02396.
[29] J. Hwang, et al., van der Waals Epitaxial Growth of Graphene on Sapphire by Chemical Vapor Deposition without a Metal Catalyst, ACS Nano 7 (2013) 385.
[30] N. Blanc, J. Coraux, C. Vo-Van, A.T. N'Diaye, O. Geaymond, G. Renaud, Local deformations and incommensurability of high-quality epitaxial graphene on a weakly interacting transition metal, Phys. Rev. B 86 (2012) 235439.

[31] K.L.W. Lau, K.M. Yu, D. Luo, R.S. Ruoff, M.S. Altman, High throughput scanning μLEED imaging of surface structural heterogeneity: defective graphene on Cu(111), Ultramicroscopy 200 (2019) 67.
[32] M. Henzler, Capabilities of LEED for defect analysis, Surf. Rev. Lett. 4 (1997) 489.
[33] F. Liu, et al., Co-field-reconciled direct growth of 6-inch monolayer graphene, Natl. Sci. Rev. 13 (2026) nwaf562.
[34] S.T. Chui, J.D. Weeks, Dynamics of the roughening transition, Phys. Rev. Lett. 40 (1978) 733.
[35] P. Nozières, F. Gallet, The roughening transition of crystal surfaces. I. static and dynamic renormalization theory, crystal shape and facet growth, J. Phys. 48 (1987) 353.
[36] M. Uwaha, Introduction to the BCF theory, Prog. Cryst. Growth Char. Mater. 62 (2016) 58.
[37] W.K. Burton, N. Cabrera, F.C. Frank, The growth of crystals and the equilibrium structure of their surfaces, Philos. Trans. R. Soc. Lond. Ser. Math. Phys. Sci. 243 (1951) 299.
[38] M. Kardar, G. Parisi, Y.-C. Zhang, Dynamic scaling of growing interfaces, Phys. Rev. Lett. 56 (1986) 889.
[39] H. Hibino, H. Kageshima, F. Maeda, M. Nagase, Y. Kobayashi, H. Yamaguchi, Microscopic thickness determination of thin graphite films formed on SiC from quantized oscillation in reflectivity of low-energy electrons, Phys. Rev. B Condens. Matter 77 (2008) 1.
[40] R.M. Feenstra, M. Widom, Low-energy electron reflectivity from graphene: first-principles computations and approximate models, Ultramicroscopy 130 (2013) 101.
[41] K.V. Bets, N. Gupta, B.I. Yakobson, How the complementarity at vicinal steps enables growth of 2D monocrystals, Nano Lett. 19 (2019) 2027.
[42] V.I. Artyukhov, Y. Hao, R.S. Ruoff, B.I. Yakobson, Breaking of symmetry in graphene growth on metal substrates, Phys. Rev. Lett. 114 (2015) 115502.
[43] V.I. Artyukhov, Y. Liu, B.I. Yakobson, Equilibrium at the edge and atomistic mechanisms of graphene growth, Proc. Natl. Acad. Sci. 109 (2012) 15136.
[44] L. Sun, et al., Hetero-site nucleation for growing twisted bilayer graphene with a wide range of twist angles, Nat. Commun. 12 (2021) 2391.
[45] Y. Li, H. Liu, Z. Chang, H. Li, S. Wang, L. Lin, H. Peng, Y. Wei, L. Sun, Z. Liu, Slip-line-guided growth of graphene, Adv. Mater. 34 (2022) 2201188.
[46] C. Wu, et al., Restoring ultra-flat bridgman-fabricated single-crystal Cu(111) wafers via recrystallization arrest strategy for high-quality graphene epitaxy, Adv. Mater. 37 (2025) 2501582.